Discrétisations conformes des solutions aux éléments de frontière du problème direct en électroencéphalographie

Original
Discrétisations conformes des solutions aux éléments de frontière du problème direct en électroencéphalographie / Rahmouni, L., Adrian, S.B., Cools, K., Andriulli, F.P.. - In: COMPTES RENDUS PHYSIQUE. - ISSN 1631-0705. - 19:1-2(2018), pp. 7-25. [10.1016/j.crhy.2018.02.002]

Publisher:
Elsevier Masson SAS

Published
DOI:10.1016/j.crhy.2018.02.002

C. R. Physique 19 (2018) 7–25

Contents lists available at ScienceDirect

Comptes Rendus Physique

www.sciencedirect.com

Radio science for Humanity / Radiosciences au service de l'humanité

Conforming discretizations of boundary element solutions to the electroencephalography forward problem

Discrétisations conformes des solutions aux éléments de frontière du problème direct en électroencéphalographie

Lyes Rahmouni [a,*], Simon B. Adrian [a,b], Kristof Cools [c], Francesco P. Andriulli [a,d,*]

[a] *IMT Atlantique, Technopole Brest-Iroise, 29238 Brest, France*
[b] *Technische Universität München, Arcisstr. 21, 80333 München, Germany*
[c] *The University of Nottingham, University Park, Nottingham, NG7 2RD, UK*
[d] *Politecnico di Torino, corso Duca degli Abruzzi 24, 10129 Torino, Italy*

ARTICLE INFO

Article history:
Available online 21 February 2018

Keywords:
EEG
Inverse problem
Forward problem
Mixed discretizations
Indirect formulation

Mots-clés :
EEG
Problème inverse
Problème direct
Discrétisation mixte
Formulation indirecte

ABSTRACT

In this paper, we present a new discretization strategy for the boundary element formulation of the Electroencephalography (EEG) forward problem. Boundary integral formulations, classically solved with the Boundary Element Method (BEM), are widely used in high resolution EEG imaging because of their recognized advantages, in several real case scenarios, in terms of numerical stability and effectiveness when compared with other differential equation based techniques. Unfortunately, however, it is widely reported in literature that the accuracy of standard BEM schemes for the forward EEG problem is often limited, especially when the current source density is dipolar and its location approaches one of the brain boundary surfaces. This is a particularly limiting problem given that during an high-resolution EEG imaging procedure, several EEG forward problem solutions are required, for which the source currents are near or on top of a boundary surface.

This work will first present an analysis of standardly and classically discretized EEG forward problem operators, reporting on a theoretical issue of some of the formulations that have been used so far in the community. We report on the fact that several standardly used discretizations of these formulations are consistent only with an L^2-framework, requiring the expansion term to be a square integrable function (i.e., in a Petrov–Galerkin scheme with expansion and testing functions). Instead, those techniques are not consistent when a more appropriate mapping in terms of fractional-order Sobolev spaces is considered. Such a mapping allows the expansion function term to be a less regular function, thus sensibly reducing the need for mesh refinements and low-precisions handling strategies that are currently required. These more favorable mappings, however, require a different and conforming discretization, which must be suitably adapted to them. In order to appropriately fulfill this requirement, we adopt a mixed discretization based on dual boundary elements residing on a suitably defined dual mesh. We devote also a particular attention to implementation-oriented details of our new technique that will allow the rapid incorporation of our finding in one's own EEG forward solution technology. We conclude by showing how the resulting forward EEG problems show favorable properties with respect

---

* Corresponding author.
E-mail addresses: lyes.rahmouni@telecom-bretagne.eu (L. Rahmouni), simon.adrian@tum.de (S.B. Adrian), Kristof.Cools@nottingham.ac.uk (K. Cools), francesco.andriulli@polito.it (F.P. Andriulli).

https://doi.org/10.1016/j.crhy.2018.02.002

to previously proposed schemes, and we show their applicability to real-case modeling scenarios obtained from Magnetic Resonance Imaging (MRI) data.

RÉSUMÉ

Dans ce papier, nous présentons une nouvelle stratégie de discrétisation pour la formulation aux éléments de frontière du problème direct de l'électroencéphalographie (EEG). Les méthodes aux éléments frontières (BEM) sont largement utilisées en imagerie EEG à haute résolution dans divers scénarios, pour leur stabilité numérique et leur efficacité reconnues par rapport à d'autres techniques basées sur des équations différentielles.

Malheureusement, il est également reconnu dans la littérature que leur précision diminue particulièrement lorsque la source de courant est dipolaire et se situe près de la surface du cerveau. Ce défaut constitue une importante limitation, étant donné qu'au cours d'une session d'imagerie EEG à haute résolution, plusieurs solutions du problème direct EEG sont requises, pour lesquelles les sources de courant sont proches ou sur la surface de cerveau.

Ce travail présente d'abord une analyse des opérateurs intervenant dans le problème direct et leur discrétisation. Nous montrons que plusieurs discrétisations couramment utilisées ne conviennent que dans un cadre L^2, nécessitant que le terme d'expansion soit une fonction de carré intégrable. Dès lors, ces techniques ne sont pas cohérentes avec les propriétés spectrales des opérateurs en termes d'espaces de Sobolev d'ordre fractionnaire.

Nous développons ensuite une nouvelle stratégie de discrétisation conforme aux espaces de Sobolev avec des fonctions d'expansion moins régulières, donnant lieu à une nouvelle formulation intégrale. Le solveur résultant présente des propriétés favorables par rapport aux méthodes existantes et réduit sensiblement le recours à un maillage adaptatif et autres stratégies actuellement requises pour améliorer la précision du calcul. Les résultats numériques présentés corroborent les développements théoriques et mettent en évidence l'impact positif de la nouvelle approche.

State-of-the-art high-resolution Electroencephalography (EEG) can righteously be considered a fully fledged imaging technique for the brain [1]. Its high temporal resolution, together with the compatibility and complementarity with other imaging strategies – Magnetoencephalography (MEG), Positron Emission Tomography (PET), and Magnetic Resonance Imaging (MRI) – [2–5], explains the steady interest that EEG is attracting in neuroimaging [6–8]. The peculiarity of high-resolution EEGs with respect to the traditional analyses based on grapho-elements, is the reconstruction of the volume brain sources based on scalp potential data [9,10]. This is the EEG inverse source problem, which is, as it is well known, ill-posed [11]. The solution to the EEG inverse source problem relies on multiple iterated solutions to the EEG forward problem where, known the configuration of brain sources, the electric potential is recovered at the scalp [12]. The accuracy in the solution to the EEG forward problem clearly impacts and limits the accuracy of the associated EEG inverse problem: a low accuracy of the solutions to the EEG forward problem translates in a low accuracy of the inverse problem solution [13]. This results in the pressing need to keep the accuracy of the EEG forward problem as high as possible.

Among the techniques to solve the EEG forward problem, Boundary Element Method (BEM) is a widely used one [14]. This numerical strategy is based on an integral formulation equivalent to the Poisson equation and, when compared with other numerical approaches like the Finite Element Method (FEM) or the Finite Difference Method (FDM) [15], BEM based solvers only discretize the surfaces enclosing the different brain regions and do not require the use of boundary conditions to terminate the solution domain. This results in interaction matrices of a smaller dimensionality [16] and explains the popularity of the BEM approach in the scientific community. Unfortunately, standard BEM methods are no panacea. It is widely reported, in fact, that the accuracy of standard BEM schemes for the forward EEG problem is often limited, especially when the current source density is dipolar and its location approaches one of the brain boundary surfaces [17,18]. This is a particularly limiting problem given that, during the solution to the EEG inverse source problem, several forward EEG problem solutions are required for which the the primary current density terms are near or on top of a boundary surface [19,20].

Three main strategies have been reported in the literature to limit the impact of accuracy losses: (i) the avoidance of brain source modeling near boundaries [21], (ii) the use of global or local mesh refinements that can better handle the singularity of the dipolar source term [22,23,20], and (iii) the introduction of a symmetric boundary element formulation [24,25]. All the above-mentioned techniques can sensibly improve source-related precision issues, but at the same time they present some undesirable drawbacks: (i) avoiding the positioning of dipolar sources near boundaries, on the one hand, represents a limitation on correct modeling [19] and, on the other hand, it increases the ill-posedness of the inverse-source problem [26]. (ii) The use of mesh refinements increases the computational burden, due to the higher dimensionality of the refined models, and this can result in substantial inefficiencies [21,27]. This is especially true in the context of inverse source problem solutions, where sources are often equally distributed near the boundaries of brain layers [19]. (iii) The use of symmetric formulations, which are based on a clever and complete exploitation of the representation theorem, results in the simultaneous resolution of two integral equations in two unknowns, and sensibly improves the accuracy of BEM method based EEG imaging. However, these formulations result in more unknowns, which increases the computational complexity of the EEG forward and inverse solutions. Moreover, the symmetric formulation in [24,25] presents a conditioning that is dependent on and growing with the number of unknowns (or equivalently with the inverse of the mesh parameter). This ill-conditioning results in harder-to-obtain numerical solutions to realistic problems as the matrix inversion becomes an increasingly unstable operation [28].

To circumvent the above-mentioned limitations, this work proposes a different approach. We first start from analyzing the mapping properties of standard EEG forward problem operators (double and adjoint double layer). We report on the fact that standardly used discretizations of these operators are consistent only with an L^2-formulation, requiring the expansion term to be a square integrable function. Instead, those techniques are not consistent when a mapping in terms of fractional-order Sobolev spaces is considered. Such a mapping, in the case of the adjoint double layer operator, would allow the expansion term to be a less regular function, sensibly reducing the need for mesh refinements and low-precisions handling strategies currently required. These more favorable mappings, however, require a different and conforming discretization that must be suitably adapted to them. Some of the authors of this work presented in the past a strategy to comply with proper Sobolev space mappings based on dual elements. This approach was introduced in [29] and named "mixed discretization". Mixed discretizations are conforming with respect to Sobolev properties of second kind operators. This approach has been subsequently applied to several problems in electromagnetics [30,31] and acoustics [32]. In this work, we have applied the mixed discretization concept to the case of multi-layered EEG operators used to solve piecewise homogeneous and isotropic nested head models. This discretization strategy can be extended to non-nested topologies. The resulting forward EEG problems show favorable properties with respect to previously proposed schemes. As a complement to the theoretical and numerical treatments, a particular attention has been devoted to implementation-oriented details that will allow the specialized practitioner to easily incorporate these findings in his EEG forward solution technology. Very preliminary and partial results of this contribution have been presented in a conference contribution [33].

This paper is organized as follows: in Section 1 we first review classical EEG discretizations and we analyze their consistency with respect to fractional-order Sobolev space mappings; we then introduce dual basis functions and the new forward EEG mixed discretized formulations we propose in this work. Following this, we develop a new robust integral representation which features high accuracy even when the conductivity ratio is high. In Section 3, we present a complete numerical study of the new techniques to comparatively test their performance against the state of the art. This will be done on both canonical spherical models (for which benchmarking against analytic solutions is possible) and on realistic models arising from MRI data. Section 4 presents our discussion of these results and our conclusions.

1. Methods

1.1. Standard integral equation formulations of the electroencephalography forward problem

Let σ be a smooth, isotropic conductivity distribution and let $\boldsymbol{j}$ be a quasi-static electric volume current density distribution in $\mathbb{R}^3$. The current density $\boldsymbol{j}$ generates the electric potential ϕ, a relationship that is mathematically expressed by the Poisson's equation

$$\nabla \cdot \sigma \nabla \phi = f = \nabla \cdot \boldsymbol{j}, \quad \text{in } \mathbb{R}^3 \tag{1}$$

When σ models the conductivity distribution of a human head, the problem of finding the electric potential ϕ is denoted as the EEG forward problem [14,11].

In BEM techniques, the head is usually modeled by domains of different areas of constant conductivity. The conductivity σ is a piecewise constant function dividing the space $\mathbb{R}^3$ in a nested sequence of regions as depicted in Fig. 1. The different domains corresponding to the regions where σ is constant and equal to σ_i are labeled Ω_i with $i = 1, \ldots, N+1$. The domain Ω_{N+1} is the exterior region, extending to infinity, with $\sigma_{N+1} = 0$. In Ω_{N+1} no current sources are present. The surfaces separating the different regions of conductivity are labeled Γ_i with $i = 1, \ldots, N$ as shown in Fig. 1.

In order to account for piecewise continuous σ, Eq. (1) must be complemented by transmission and boundary conditions resulting in [34]

$$\sigma_i \Delta \phi = f \quad \text{in } \Omega_i, \quad \text{for all } i = 1, \ldots, N \tag{2}$$

$$\Delta \phi = 0 \quad \text{in } \Omega_{N+1} \tag{3}$$

$$[\phi]_j = 0 \quad \text{on } \Gamma_j, \text{ for all } j = 1, \ldots, N \tag{4}$$

$$[\sigma \partial_{\hat{\boldsymbol{n}}} \phi]_j = 0 \quad \text{on } \Gamma_j, \text{ for all } j = 1, \ldots, N \tag{5}$$

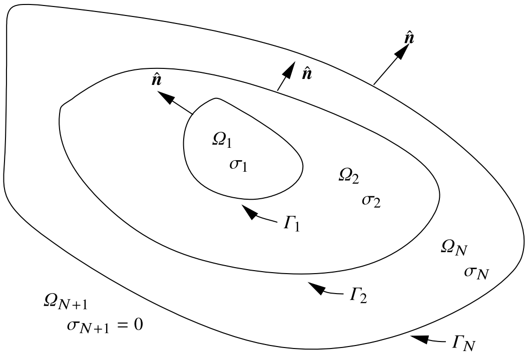

Fig. 1. Nested sequences of regions with constant conductivity.

The expression $[g]_j$ denotes the jump of the function g at the surface Γ_j, that is,

$$[g]_j = g|^-_{\Gamma_j} - g|^+_{\Gamma_j} \tag{6}$$

with $g|^-_{\Gamma_j}$ and $g|^+_{\Gamma_j}$ the interior and exterior limits of g at the surface Γ_j, respectively. These limits are defined as

$$g|^{\pm}_{\Gamma_j}(\boldsymbol{r}) := \lim_{\alpha\to 0^{\pm}} g(\boldsymbol{r} + \alpha\hat{\boldsymbol{n}}) \quad \text{for all } \boldsymbol{r} \text{ on } \Gamma_j \tag{7}$$

where $\hat{\boldsymbol{n}}$ denotes the normal at each surface (see Fig. 1).

1.1.1. *Boundary integral operators*

Boundary element methods provide a numerical approximation of the potential ϕ [35,36] when the forward EEG problem is cast in an integral equation formulation. In the following, we introduce the integral operators and their mapping properties, and we review the standard integral formulations of the EEG forward problem.

Definition 1 *(Boundary integral operators).* Let $\Omega \subset \mathbb{R}^3$ be a bounded Lipschitz domain with boundary $\Gamma := \partial\Omega$. We define the single layer operator

$$\mathcal{S} : H^{-1/2}(\Gamma) \to H^{1/2}(\Gamma), \qquad (\mathcal{S}u)(\boldsymbol{r}) = \int_{\Gamma} G(\boldsymbol{r} - \boldsymbol{r}')u(\boldsymbol{r}')\mathrm{d}S(\boldsymbol{r}') \tag{8}$$

the double layer and adjoint double layer operator

$$\mathcal{D} : H^{1/2}(\Gamma) \to H^{1/2}(\Gamma)\,, \qquad (\mathcal{D}u)(\boldsymbol{r}) := \int_{\Gamma} \partial_{\hat{\mathbf{n}}'} G(\boldsymbol{r} - \boldsymbol{r}')u(\boldsymbol{r}')\mathrm{d}S(\boldsymbol{r}') \tag{9}$$

$$\mathcal{D}^* : H^{-1/2}(\Gamma) \to H^{-1/2}(\Gamma)\,, \qquad (\mathcal{D}^*u)(\boldsymbol{r}) = \int_{\Gamma} \partial_{\hat{\mathbf{n}}} G(\boldsymbol{r} - \boldsymbol{r}')u(\boldsymbol{r}')\mathrm{d}S(\boldsymbol{r}') \tag{10}$$

and the hypersingular operator

$$\mathcal{N} : H^{1/2}(\Gamma) \to H^{-1/2}(\Gamma)\,, \qquad (\mathcal{N}u)(\boldsymbol{r}) = \int_{\Gamma} \partial_{\hat{\mathbf{n}},\hat{\mathbf{n}}'} G(\boldsymbol{r} - \boldsymbol{r}')u(\boldsymbol{r})\mathrm{d}S(\boldsymbol{r}') \tag{11}$$

In the definitions above, the function

$$G(\boldsymbol{r} - \boldsymbol{r}') = \frac{1}{4\pi|\boldsymbol{r} - \boldsymbol{r}'|} \tag{12}$$

is the free-space Green's function. The Sobolev spaces H^x, $x \in \{-1/2, 1/2\}$, appearing in the mapping properties are briefly defined in Appendix A.

Remark. The reader should be warned that there is no consistent naming of the operators above in the literature and the naming choice made here is the one classically adopted in potential theory (see for example [28]).

Source modeling and inhomogeneous solution Current dipoles are a common approximation of brain electric sources making them a widely used model in the forward and inverse EEG problem [37–39]. The current dipole is defined by

$$\boldsymbol{j}_{\mathrm{dip}}(\boldsymbol{r}) = \boldsymbol{q}\delta_{\boldsymbol{r}_0}(\boldsymbol{r}) \tag{13}$$

where $\boldsymbol{q}$ represents the dipole moment and $\delta_{\boldsymbol{r}_0}$ the Dirac delta function. The corresponding potential in an infinite homogeneous domain is

$$v_{\mathrm{dip}}(\boldsymbol{r}) = \frac{1}{4\pi}\frac{\boldsymbol{q}\cdot(\boldsymbol{r}-\boldsymbol{r}_0)}{|\boldsymbol{r}-\boldsymbol{r}_0|^3} \tag{14}$$

Throughout the following sections, we use

$$v_{\mathrm{s},\Omega_i} = v_{\mathrm{dip}} \quad \text{for } \boldsymbol{r}_0 \in \Omega_i \tag{15}$$

Moreover, whenever two underscore indices j, i are added to an operator symbol we mean that, in defining the operator, the integration is constrained to the ith surface and the integral is evaluated only on the jth surface. For example, $\mathcal{S}_{ji}$ is defined as

$$(\mathcal{S}_{ji}p)(\boldsymbol{r}) = \int\limits_{\Gamma_i} G(\boldsymbol{r}-\boldsymbol{r}')p(\boldsymbol{r}')\mathrm{d}S(\boldsymbol{r}'), \quad \boldsymbol{r}\in\Gamma_j \tag{16}$$

1.1.2. Boundary integral formulations

Three integral formulations are commonly used for computing the electric potential ϕ in Eq. (1) [25,40–42]. All of them leverage the same principle: the electric potential ϕ is decomposed into

$$\phi = v_{\mathrm{s}} + v_{\mathrm{h}} \tag{17}$$

such that $\sigma_i \Delta v_{\mathrm{s}} = f$ in Ω_i for all $i = 1, \ldots, N$ (see Eq. (2)) and such that v_{h} is a piecewise harmonic correction ensuring that ϕ will satisfy the boundary conditions (4) and (5). For setting the notation and for the sake of self-consistency, we list these formulations below; for a more detailed derivation, we refer the reader to [25] and references therein.

The adjoint double layer formulation. In this formulation, the ansatz for v_{s1} has the following form:

$$v_{\mathrm{s1}} = \sum_{i=1}^{N}\frac{v_{\mathrm{s},\Omega_i}}{\sigma_{\mathrm{i}}} \tag{18}$$

This choice satisfies Eq. (2) and Eq. (3), and in addition, $[v_{\mathrm{s1}}]_j = 0$ and $[\partial_{\hat{\boldsymbol{n}}} v_{\mathrm{s1}}]_j = 0$. Theorem 1 in Appendix B is then used to construct a harmonic function a v_{h1} such that a Neumann's boundary condition is satisfied. It is obtained that

$$\partial_{\hat{\boldsymbol{n}}} v_{\mathrm{s1}}|_{\Gamma_j} = \frac{\sigma_j + \sigma_{j+1}}{2(\sigma_{j+1}-\sigma_j)}q_{\Gamma_j} - \sum_{i=1}^{N}\mathcal{D}^*_{ji}q_{\Gamma_i} \quad \text{for } j = 1, \ldots, N \tag{19}$$

The double layer formulation. The following particular solution is put forward (see, for example, [25] or [40])

$$v_{\mathrm{s2}} = \sum_{i=1}^{N} v_{\mathrm{s},\Omega_i} \tag{20}$$

which satisfies Eq. (2), $[v_{\mathrm{s2}}] = 0$, and $[\partial_{\hat{\boldsymbol{n}}} v_{\mathrm{s2}}] = 0$. After complementing it with a harmonic solution v_{h2} that satisfies, $[\partial_{\hat{\boldsymbol{n}}} v_{\mathrm{h2}}] = 0$, it is obtained

$$v_{\mathrm{s2}}|_{\Gamma_j} = \frac{\sigma_j + \sigma_{j+1}}{2}\phi_{\Gamma_j} - \sum_{i=1}^{N}(\sigma_{i+1}-\sigma_i)\mathcal{D}_{ji}\phi_{\Gamma_i} \tag{21}$$

The symmetric formulation. Differently from the previous two approaches, in the symmetric formulation, the harmonic function v_{h3} is constructed as follows [25]

$$v_{\mathrm{h3},\Omega_i} = \begin{cases} \phi - \frac{v_{\mathrm{s},\Omega_i}}{\sigma_i}, & \text{in } \Omega_i \\ -\frac{v_{\mathrm{s},\Omega_i}}{\sigma_i}, & \text{in } \mathbb{R}^3 \setminus \overline{\Omega}_i \end{cases} \tag{22}$$

Then, it can be shown that

$$\begin{aligned} &\sigma_{i+1}^{-1}(v_{\mathrm{s},\Omega_{i+1}})\big|_{\Gamma_i} - \sigma_i^{-1}(v_{\mathrm{s},\Omega_i})\big|_{\Gamma_i} \\ &\quad = \mathcal{D}_{i,i-1}\phi_{\Gamma_{i-1}} - 2\mathcal{D}_{ii}\phi_{\Gamma_i} + \mathcal{D}_{i,i+1}\phi_{\Gamma_{i+1}} - \sigma_i^{-1}\mathcal{S}_{i,i-1}d_{\Gamma_{i-1}} + (\sigma_i^{-1}+\sigma_{i+1}^{-1})\mathcal{S}_{ii}d_{\Gamma_i} - \sigma_{i+1}^{-1}\mathcal{S}_{i,i+1}d_{\Gamma_{i+1}} \end{aligned} \tag{23}$$

and

$$(\partial_{\hat{\boldsymbol{n}}} v_{\mathrm{s},\Omega_{i+1}})\big|_{\Gamma_i} - (\partial_{\hat{\boldsymbol{n}}} v_{\mathrm{s},\Omega_i})\big|_{\Gamma_i}$$
$$= \sigma_i \mathcal{N}_{i,i-1}\phi_{\Gamma_{i-1}} - (\sigma_i + \sigma_{i+1})\mathcal{N}_{ii}\phi_{\Gamma_i} + \sigma_{i+1}\mathcal{N}_{i,i+1}\phi_{\Gamma_{i+1}} - \mathcal{D}^*_{i,i-1} d_{\Gamma_{i-1}} + 2\mathcal{D}^*_{ii} d_{\Gamma_i} - \mathcal{D}^*_{i,i+1} d_{\Gamma_{i+1}} \tag{24}$$

hold for $i = 1, \ldots, N$. Here we have used the notation $d_{\Gamma_i} = \sigma_i \partial_{\hat{\boldsymbol{n}}}\phi|^-_{\Gamma_i}$.

1.2. Analysis of the main drawbacks of standard discretizations

To evidence the drawbacks of standard (currently used in literature) BEM discretizations of the EEG forward problem, we have to consider Petrov–Galerkin theory, which provides the convergence properties of a numerical boundary element solution in the case of asymmetric discretizations [36].

1.2.1. Petrov–Galerkin method reviewed

Let X and Y be Hilbert spaces, and $\mathcal{A}: X \to Y'$ a bounded, linear operator. We can associate with $\mathcal{A}$ a bilinear form $a: X \times Y \to \mathbb{R}$ that satisfies $|a(x,y)| \leq C\,\|x\|_X\,\|y\|_Y$ with $C > 0$. We are faced with the variational problem to find $u \in X$ such that $a(u,v) = \langle f, v\rangle_{Y' \times Y}$ for all $v \in Y$ with $f \in Y'$.

To solve this variational formulation, we cast this problem into a matrix-vector equation by using finite-dimensional subspaces $X_h \subset X$ and $Y_h \subset Y$ with $\dim(X_h) = \dim(Y_h) = M$. The task is to find $u_h \in X_h$ such that $a(u_h, v_h) = \langle f, v_h\rangle_{Y'_h \times Y_h}$ for all $v_h \in Y_h$. The function u_h is an approximation of u and this approach is called the Petrov–Galerkin method [36].

The key ingredient of the Petrov–Galerkin method is that the testing is always performed in the dual space of the range of $\mathcal{A}$, where we notice that $Y'' = Y$ because of the reflexivity of Y.

1.2.2. Standard discretizations

The classical integral equations presented in Section 1.1.2 are discretized using a BEM approach. The different regions Ω_i of the head are approximated with polygonal domains. On these domains, meshes are generated by using a triangular tessellation. The potential ϕ is approximated by a linear combination of expansion functions $\alpha_i \in X_\alpha$, i.e.

$$\phi \approx \sum_{j=1}^{N_\alpha} c_j \alpha_j \quad \text{for } \boldsymbol{r} \in \bigcup_i \Gamma_i \tag{25}$$

where c_j are the (unknown) expansion coefficients, and $N_\alpha = \dim X_\alpha$ is the dimensionality of the function space X_α.

Commonly used functions are the piecewise constant functions (PCFs) p_j (also referred to as patch functions) and piecewise linear functions (PLFs) λ_j (also referred to as linear Lagrangian or pyramid functions). These functions form the boundary element spaces $\operatorname{span}\{p_j\}_{j=1}^{N_\mathrm{p}} =: X_\mathrm{p}$ and $\operatorname{span}\{\lambda_j\}_{j=1}^{N_\lambda} =: X_\lambda$ and it holds that $X_\mathrm{p} \subset H^{-1/2}$ and $X_\lambda \subset H^{1/2}$ [36]. Both the PCFs and the PLFs form a partition of unity.

We denote the system matrix that stems from the discretization of an operator $\mathcal{X}$ with the expansion functions α_j and testing functions β_i as $\boldsymbol{X}_{\beta\alpha}$ with

$$[\boldsymbol{X}_{\beta\alpha}]_{ij} = (\beta_i, \mathcal{X}\alpha_j)_{L^2} \tag{26}$$

This notation is necessary, as some operators are discretized with different expansion and testing functions.

A standard discretization in the literature for the adjoint double layer and double layer formulation is the one where PCFs are used as expansion and testing functions [25,40]. Using the notation of Eq. (26), such a discretization for the adjoint double layer formulation would read

$$\boldsymbol{I}_{k,\mathrm{pp}} - \boldsymbol{D}^*_{kl,\mathrm{pp}} = \boldsymbol{v}_{\mathrm{s}1,k,\mathrm{p}} \quad k,l = 1,\ldots,N \tag{27}$$

where

$$[\boldsymbol{I}_{k,\mathrm{pp}}]_{ij} = \frac{\sigma_k + \sigma_{k+1}}{2(\sigma_{k+1} - \sigma_k)} (p_i^{(k)}, p_j^{(k)})_{L^2(\Gamma_k)} \tag{28}$$

$$[\boldsymbol{D}^*_{kl,\mathrm{pp}}]_{ij} = (p_i^{(k)}, \mathcal{D}^*_{kl}\, p_j^{(l)})_{L^2(\Gamma_k)} \tag{29}$$

$$[\boldsymbol{v}_{\mathrm{s}1,k,\mathrm{p}}]_i = (p_i^{(k)}, \partial_{\hat{\boldsymbol{n}}} v_{\mathrm{s}1})_{L^2(\Gamma_k)} \tag{30}$$

and $q_{\Gamma_k} \approx \sum_i [\boldsymbol{q}_{k,\mathrm{p}}]_i\, p_i^{(k)}$.

The Petrov–Galerkin theory reviewed in the previous section, however, prohibits the use of PCFs as testing functions since on the right-hand-side we have the sum of the identity operator $\mathcal{I}$ and the adjoint double layer operator $\mathcal{D}^*$ terms. Since $\mathcal{I}: H^{-1/2} \to H^{-1/2}$, the entire right-hand side is a (bijective) mapping from $H^{-1/2}$ to $H^{-1/2}$. The dual space of the range is $H^{1/2}$. As $X_{\mathrm{p}} \nsubseteq H^{1/2}$, we cannot use PCFs as testing functions: they are not regular enough and thus the commonly used discretization of the operator in Eq. (27) is incompatible with the mapping $H^{-1/2} \to H^{-1/2}$ of the operator.

Also the classical discretization for the double layer formulation (Eq. (21)) is leveraging on PCF both as expansion and testing functions, i.e.

$$\boldsymbol{J}_{k,\mathrm{pp}} + \zeta_l \boldsymbol{D}_{kl,\mathrm{pp}} = \boldsymbol{v}_{\mathrm{s}2,k,\mathrm{p}} \quad k,l = 1,\ldots,N \tag{31}$$

where

$$[\boldsymbol{J}_{k,\mathrm{pp}}]_{ij} = \frac{\sigma_k + \sigma_{k+1}}{2} (p_i^{(k)}, p_j^{(k)})_{L^2(\Gamma_k)} \tag{32}$$

$$[\boldsymbol{D}_{kl,\mathrm{pp}}]_{ij} = (p_i^{(k)}, \mathcal{D}_{kl}\, p_j^{(l)})_{L^2(\Gamma_k)} \tag{33}$$

$$[\boldsymbol{v}_{\mathrm{s}2,k,\mathrm{p}}]_i = -(p_i^{(k)}, v_{\mathrm{s}2})_{L^2(\Gamma)_k} \tag{34}$$

and $\phi_{\Gamma_k} \approx \sum_i [\boldsymbol{\phi}_{k,\mathrm{p}}]_i p_i^{(k)}$ and $\zeta_l = -(\sigma_{l+1} - \sigma_l)$. For the double layer formulation (Eq. (31)), we find that the operator on the left-hand side is a mapping $H^{1/2} \to H^{1/2}$, since $\mathcal{I}$ maps from $H^{1/2}$ to $H^{1/2}$. The relationship $X_{\mathrm{p}} \nsubseteq H^{1/2}$ implies that the use of PCFs as expansion functions is forbidden. More regular expansion functions must be used.

The standard discretization of the symmetric formulation reads [25]

$$-\sigma_k \boldsymbol{N}_{kk-1,\lambda\lambda} + \boldsymbol{D}^*_{kk-1,\lambda\mathrm{p}} + \eta_k \boldsymbol{N}_{kk,\lambda\lambda} - 2\boldsymbol{D}^*_{kk,\lambda\mathrm{p}} - \sigma_{k+1} \boldsymbol{N}_{kk+1,\lambda\lambda} + \boldsymbol{D}^*_{kk+1,\lambda\mathrm{p}} = \boldsymbol{v}_{\mathrm{sym},k,\lambda} \tag{35}$$

$$\boldsymbol{D}_{kk-1,\mathrm{p}\lambda} - \sigma_k^{-1} \boldsymbol{S}_{kk-1,\mathrm{pp}} - 2\boldsymbol{D}_{kk,\mathrm{p}\lambda} + \theta_k \boldsymbol{S}_{kk,\mathrm{pp}} + \boldsymbol{D}_{kk+1,\mathrm{p}\lambda} - \sigma_{k+1}^{-1} \boldsymbol{S}_{kk+1,\mathrm{pp}} = \boldsymbol{p}_{\mathrm{sym},k,\mathrm{p}} \tag{36}$$

where

$$[\boldsymbol{N}_{kl,\lambda\lambda}]_{ij} = (\lambda_i^{(k)}, \mathcal{N}_{kl} \lambda_j^{(l)})_{L^2(\Gamma_k)} \tag{37}$$

$$[\boldsymbol{S}_{kl,\mathrm{pp}}] = (p_i^{(k)}, \mathcal{S}_{kl} p_j^{(l)})_{L^2(\Gamma_k)} \tag{38}$$

$$[\boldsymbol{D}_{kl,\mathrm{p}\lambda}]_{ij} = (p_i^{(k)}, \mathcal{D}_{kl} \lambda_j^{(l)})_{L^2(\Gamma_k)} \tag{39}$$

$$[\boldsymbol{D}^*_{kl,\lambda\mathrm{p}}]_{ij} = (\lambda_i^{(k)}, \mathcal{D}^*_{kl} p_j^{(l)})_{L^2(\Gamma_k)} \tag{40}$$

$$[\boldsymbol{v}_{\mathrm{sym},k,\lambda}]_i = (\lambda_i^{(k)}, \sigma_{k+1}^{-1} (v_{\mathrm{s},\Omega_{k+1}})\big|_{\Gamma_k} - \sigma_k^{-1} (v_{\mathrm{s},\Omega_k})\big|_{\Gamma_k})_{L^2} \tag{41}$$

$$[\boldsymbol{p}_{\mathrm{sym},k,\mathrm{p}}]_i = (p_i^{(k)}, (\partial_{\hat{\boldsymbol{n}}} v_{\mathrm{s},\Omega_{k+1}})\big|_{\Gamma_k} - (\partial_{\hat{\boldsymbol{n}}} v_{\mathrm{s},\Omega_k})\big|_{\Gamma_k})_{L^2} \tag{42}$$

with $\eta_i = \sigma_i + \sigma_{i+1}$, $\theta_i = \sigma_i^{-1} + \sigma_{i+1}^{-1}$, $\phi_{\Gamma_k} \approx \sum_i [\boldsymbol{\phi}_{k,\lambda}]_i \lambda_i^{(k)}$, and $d_{\Gamma_k} \approx \sum_i [\boldsymbol{\phi}_{k,\mathrm{p}}]_i p_i^{(k)}$. In contrast to the classical discretizations of the double layer and adjoint double layer operators, the symmetric formulation in [25] is discretized in a way that is completely conforming with respect to the fractional-order Sobolev space mappings. The single-layer operator $\mathcal{S}_{ij}$ maps from $H^{-1/2}$ to $H^{1/2}$ and thus the dual of its range is the space $H^{-1/2}$, allowing the use of PCFs as expansion and testing functions (see Eq. (41)). The hypersingular operator $\mathcal{N}_{ij}$ is discretized with PLFs as both expansion and testing functions, since the derivatives render the usage of PCFs impossible (see Eq. (35)). This is a conforming choice given that a lower regularity would not be allowed since $\mathcal{N}_{ij}$ is a mapping from $H^{1/2}$ to $H^{-1/2}$ and thus both expansion and testing functions should belong at least to $H^{1/2}$. Similar arguments can be used to show the conformity of the expansion and testing function choices for $\mathcal{D}_{ij}$ and $\mathcal{D}^*_{ij}$ in Eq. (39) and Eq. (40), respectively.

Furthermore, while the double layer and the adjoint double layer approaches give rise to a dense matrices, the matrices obtained from the symmetric approach are band diagonal. The entries of the matrix of the symmetric approach include only the interaction between adjacent compartments, which consequently reduces the computational cost.

Yet, the symmetric approach has two drawbacks: its discretization gives rise to a matrix that is one and half times the size of the matrices of the previous two approaches and, since the symmetric formulation operator is of the first kind, the resulting matrix is ill-conditioned (when the number of unknowns is increased by decreasing the average edge length h, the condition number grows unbounded [43]). We note that the double layer and adjoint double layer formulations are Fredholm integral equations of the second kind [44]. This kind of equations gives rise to well-conditioned systems.

Higher-order functions could be used to solve the above-mentioned problems in standard discretizations of the double and adjoint double layer operator. For example, given that the PLFs belong to the space $H^{1/2}$ and this space itself is a subset of the space $H^{-1/2}$, one could think of using PLFs as expansion and testing functions in Eq. (27) and Eq. (31). Although this leads to a conforming testing, it results in schemes that have either expansion or testing functions more regular than necessary, which can slow down the convergence of the approximate solution to the exact solution as h decreases; this effect is especially notable in the presence of irregular geometries such as highly realistic phantoms of the human head. Moreover, the usage of PLFs increases the computational burden: the handling of the singularity of the Green's function [45–47] in the integration routines becomes computationally more expensive and more difficult to implement.

Table 1
The abbreviations and discretizations of the standard formulations.

Label	Formulation	Function		Drawbacks
		Expansion	Testing	
Standard discretizations				
1Aa	Adjoint double layer	p	p	UR for testing
1Ab	Adjoint double layer	λ	λ	ER for expansion
1Ba	Double layer	p	p	UR for expansion
1Bb	Double layer	λ	λ	ER for testing
1C	Symmetric	p, λ	p, λ	Double-sized and ill-conditioned system matrix

ER: Excessive regularity
UR: Insufficient regularity

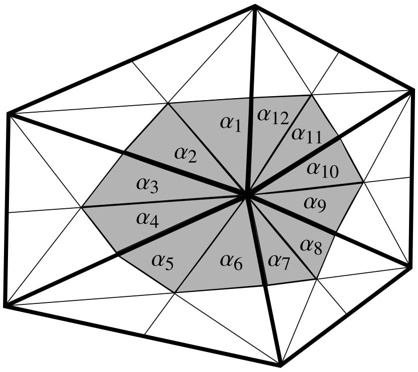

Fig. 2. The standard (thick lines) and the barycentrically refined (thin lines) mesh. The grey area is a dual cell.

Summarizing, the standard low-order discretizations of the EEG forward problem do not comply with the EEG operators requirements in terms of regularity and can lead to erroneous solutions, while the symmetric formulation is correctly discretized, but requires four times the memory space and it is an ill-conditioned formulation. The problem could be ameliorated by higher-order functions, but this increases the computational burden, and it is more complicated to implement. The above considerations are summarized in Table 1.

1.3. New mixed discretized EEG formulations

A joint application of PCFs and PLFs is not possible without getting a rectangular matrix – owing to the fact that the number of PCFs N_{p} equals the number of cells of the mesh N_{Cells}, while the number of PLFs N_{λ} equals the number of inner nodes N_{Nodes} of the mesh.

We must use a new set of PCFs and PLFs whose span has the right dimension. Such functions can be constructed by using the dual mesh, that is, the mesh where the nodes of the original mesh become cells and vice versa. In the following, we refer to these functions as Dual Piecewise Constant Functions (DPCFs) $\widetilde{p}_i$ and Dual Piecewise Linear Functions (DPLFs) $\widetilde{\lambda}_i$, and they form the spaces $X_{\widetilde{\mathrm{p}}}$ and $X_{\widetilde{\lambda}}$.

The dual mesh is obtained by barycentrically refining a standard triangular mesh: each triangle is split into six subtriangles by connecting the midpoints of each edge with the opposite node. This is shown in Fig. 2, where the original cells are those with bold edges. The union of the greyed cells around the center node of this figure form the dual cell.

In the following, a mixed discretization scheme for the EEG-based forward problem is proposed. The operators are discretized and tested in a conforming way with respect to Sobolev space mapping properties. Mixed and conforming discretization techniques were introduced by [29] in the context of full-wave solutions to scattering problems. These discretizations make use of suitably chosen dual functions. There are several ways to define these dual functions. In this work, we adopt the functions proposed in [48] in the context of Calderon preconditioning of scattering problems.

1.3.1. Dual functions

The definition of the DPCFs is simple. The support of the DPCF $\widetilde{p}_j$ is given by the cells on the barycentrically refined mesh that are attached to the jth node (Fig. 2 shows the support of a DPCF). When $\boldsymbol{r}$ is in the support of $\widetilde{p}_j$, the function value $\widetilde{p}_j(\boldsymbol{r}) = 1$ and is zero when $\boldsymbol{r}$ is not in the support of $\widetilde{p}_j$. Let p_i^{bar} be the standard PCFs defined on the barycentrically refined mesh. For the example given in Fig. 2, we find

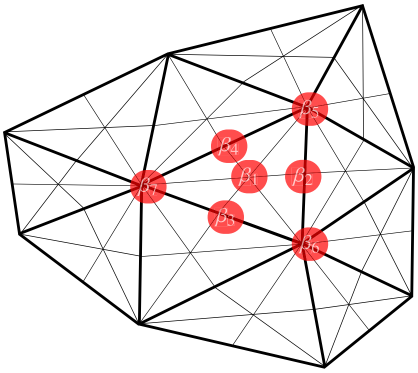

Fig. 3. Transformation matrix coefficient.

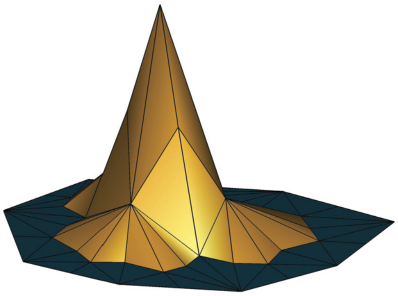

Fig. 4. An example of a typical BC piecewise linear function.

$$\widetilde{p}_j = \sum_{i=1}^{12} \alpha_i p_i^{\mathrm{bar}} \tag{43}$$

where $\alpha_i = 1$ for all $i = 1, \dots, 12$.

The function $\widetilde{\lambda}_j$ is attached to the cell j and it can be represented as a linear combination of seven standard PLFs λ_j^{bar} defined on the barycentrically refined mesh. Fig. 3 shows the general case, where the nodes of the seven relevant PLFs are labeled with the coefficients β_i that are chosen such that

$$\widetilde{\lambda}_j = \sum_{i=1}^{7} \beta_i \lambda_i^{\mathrm{bar}} \tag{44}$$

For the first coefficient, which is associated with the center PLF, we always have $\beta_1 = 1$, while for the next three coefficients, which are associated with the PLFs defined on the midpoints of the edges of the primal cell, we always have $\beta_i = 1/2$ with $i = 2, \dots, 4$. The last three coefficients β_5, β_6 and β_7, which are associated with PLFs defined on nodes of the primal cell, their weights are given by $1/N_{\mathrm{Cells},i}$ with $i = 5, \dots, 7$ and $N_{\mathrm{Cells},i}$ being the number of cells of the primal mesh that are attached to the respective node. In the example given, the coefficients are $\alpha_5 = 1/5$, $\alpha_6 = 1/6$, and $\alpha_7 = 1/6$. It can be shown that these DPLFs form a partition of unity [48]. Fig. 4 visualizes an example of a DPLF function.

1.3.2. New formulations

Following the considerations of the previous sections, we propose new mixed discretization strategies for the adjoint double layer, double layer, and symmetric approaches. For the adjoint double layer approach, we use standard PCFs as expansion and DPLFs as testing functions. This results in

$$\begin{bmatrix} \boldsymbol{I}_{1,\widetilde{\lambda}\mathrm{p}} - \boldsymbol{D}^*_{11,\widetilde{\lambda}\mathrm{p}} & -\boldsymbol{D}^*_{12,\widetilde{\lambda}\mathrm{p}} & -\boldsymbol{D}^*_{13,\widetilde{\lambda}\mathrm{p}} \\ -\boldsymbol{D}^*_{21,\widetilde{\lambda}\mathrm{p}} & \boldsymbol{I}_{2,\widetilde{\lambda}\mathrm{p}} - \boldsymbol{D}^*_{22,\widetilde{\lambda}\mathrm{p}} & -\boldsymbol{D}^*_{23,\widetilde{\lambda}\mathrm{p}} \\ -\boldsymbol{D}^*_{31,\widetilde{\lambda}\mathrm{p}} & -\boldsymbol{D}^*_{32,\widetilde{\lambda}\mathrm{p}} & \boldsymbol{I}_{3,\widetilde{\lambda}\mathrm{p}} - \boldsymbol{D}^*_{33,\widetilde{\lambda}\mathrm{p}} \end{bmatrix} \cdot \underbrace{\begin{bmatrix} \boldsymbol{q}_{1,\mathrm{p}} \\ \boldsymbol{q}_{2,\mathrm{p}} \\ \boldsymbol{q}_{3,\mathrm{p}} \end{bmatrix}}_{\boldsymbol{q}_{\mathrm{p}}} = \begin{bmatrix} \boldsymbol{v}_{\mathrm{s}1,1,\widetilde{\lambda}} \\ \boldsymbol{v}_{\mathrm{s}1,2,\widetilde{\lambda}} \\ \boldsymbol{v}_{\mathrm{s}1,3,\widetilde{\lambda}} \end{bmatrix} \tag{45}$$

where

$$[\boldsymbol{I}_{k,\widetilde{\lambda}\mathrm{p}}]_{ij} = \frac{\sigma_k + \sigma_{k+1}}{2(\sigma_{k+1} - \sigma_k)} (\widetilde{\lambda}_i^{(k)}, p_j^{(k)})_{L^2(\Gamma)} \tag{46}$$

$$[\boldsymbol{D}^*_{kl,\widetilde{\lambda}\mathrm{p}}]_{ij} = (\widetilde{\lambda}_i^{(k)}, \mathcal{D}^*_{kl}\, p_j^{(l)})_{L^2(\Gamma)} \tag{47}$$

$$[\boldsymbol{v}_{\mathrm{s1},k,\widetilde{\lambda}}]_i = (\widetilde{\lambda}_i^{(k)}, \partial_{\hat{\boldsymbol{n}}} v_{\mathrm{s1}})_{L^2(\Gamma)} \tag{48}$$

and $q_{\Gamma_k} \approx \sum_i [\boldsymbol{q}_{k,\mathrm{p}}]_i p_i^{(k)}$.

$$\begin{bmatrix} \beta_1 \boldsymbol{I}_{\widetilde{\mathrm{p}}\lambda} + \alpha_1 \boldsymbol{D}_{11,\widetilde{\mathrm{p}}\lambda} & -2\boldsymbol{S}_{11,\widetilde{\mathrm{p}}\mathrm{p}} & -\sigma_2 \boldsymbol{D}_{12,\widetilde{\mathrm{p}}\lambda} & \boldsymbol{S}_{12,\widetilde{\mathrm{p}}\mathrm{p}} & \boldsymbol{0} \\ -2\boldsymbol{N}_{11,\widetilde{\lambda}\lambda} & \delta_1 \boldsymbol{I}_{\widetilde{\lambda}\widetilde{\mathrm{p}}} + \gamma_1 \boldsymbol{D}^*_{11,\widetilde{\lambda}\mathrm{p}} & \boldsymbol{N}_{12,\widetilde{\lambda}\lambda} & -\sigma_2^{-1} \boldsymbol{D}^*_{12,\widetilde{\lambda}\mathrm{p}} & \boldsymbol{0} \\ -\sigma_2 \boldsymbol{D}_{21,\widetilde{\mathrm{p}}\lambda} & \boldsymbol{S}_{21,\widetilde{\mathrm{p}}\mathrm{p}} & \beta_2 \boldsymbol{I}_{\widetilde{\mathrm{p}}\lambda} + \alpha_2 \boldsymbol{D}_{22,\widetilde{\mathrm{p}}\lambda} & -2\boldsymbol{S}_{22,\widetilde{\mathrm{p}}\mathrm{p}} & -\sigma_3 \boldsymbol{D}_{23,\widetilde{\mathrm{p}}\lambda} \\ \boldsymbol{N}_{21,\widetilde{\lambda}\lambda} & -\sigma_2^{-1} \boldsymbol{D}^*_{21,\widetilde{\lambda}\mathrm{p}} & -2\boldsymbol{N}_{22,\widetilde{\lambda}\lambda} & \delta_2 \boldsymbol{I}_{\widetilde{\lambda}\mathrm{p}} + \gamma_2 \boldsymbol{D}^*_{22,\widetilde{\lambda}\mathrm{p}} & \boldsymbol{N}_{23,\widetilde{\lambda}\lambda} \\ \boldsymbol{0} & \boldsymbol{0} & -\sigma_3 \boldsymbol{D}_{32,\widetilde{\mathrm{p}}\lambda} & \boldsymbol{S}_{32,\widetilde{\mathrm{p}}\mathrm{p}} & \beta_3 \boldsymbol{I}_{\widetilde{\mathrm{p}}\lambda} + \alpha_3 \boldsymbol{D}_{33,\widetilde{\mathrm{p}}\lambda} \end{bmatrix} \begin{bmatrix} \boldsymbol{\phi}_{1,\lambda} \\ \boldsymbol{d}_{1,\mathrm{p}} \\ \boldsymbol{\phi}_{2,\lambda} \\ \boldsymbol{d}_{2,\mathrm{p}} \\ \boldsymbol{\phi}_{3,\lambda} \end{bmatrix}$$
$$= \begin{bmatrix} \boldsymbol{v}_{\mathrm{sym},1,\widetilde{\mathrm{p}}} \\ \boldsymbol{p}_{\mathrm{sym},1,\widetilde{\lambda}} \\ \boldsymbol{v}_{\mathrm{sym},2,\widetilde{\mathrm{p}}} \\ \boldsymbol{p}_{\mathrm{sym},2,\widetilde{\lambda}} \\ \boldsymbol{v}_{\mathrm{sym},3,\widetilde{\mathrm{p}}} \end{bmatrix} \tag{49}$$

For the double layer approach, on the other hand, we use standard PLFs as expansion and DPCFs as testing functions. The system we have to solve is

$$\begin{bmatrix} \boldsymbol{J}_{1,\widetilde{\mathrm{p}}\lambda} + \zeta_1 \boldsymbol{D}_{11,\widetilde{\mathrm{p}}\lambda} & \zeta_2 \boldsymbol{D}_{12,\widetilde{\mathrm{p}}\lambda} & \zeta_3 \boldsymbol{D}_{13,\widetilde{\mathrm{p}}\lambda} \\ \zeta_1 \boldsymbol{D}_{21,\widetilde{\mathrm{p}}\lambda} & \boldsymbol{J}_{2,\widetilde{\mathrm{p}}\lambda} + \zeta_2 \boldsymbol{D}_{22,\widetilde{\mathrm{p}}\lambda} & \zeta_3 \boldsymbol{D}_{23,\widetilde{\mathrm{p}}\lambda} \\ \zeta_1 \boldsymbol{D}_{31,\widetilde{\mathrm{p}}\lambda} & \zeta_2 \boldsymbol{D}_{32,\widetilde{\mathrm{p}}\lambda} & \boldsymbol{I}_{3,\widetilde{\mathrm{p}}\lambda} + \zeta_3 \boldsymbol{D}_{33,\widetilde{\mathrm{p}}\lambda} \end{bmatrix} \cdot \underbrace{\begin{bmatrix} \boldsymbol{\phi}_{1,\lambda} \\ \boldsymbol{\phi}_{2,\lambda} \\ \boldsymbol{\phi}_{3,\lambda} \end{bmatrix}}_{\boldsymbol{\phi}_{\mathrm{p}}} = \begin{bmatrix} \boldsymbol{v}_{\mathrm{s2},1,\widetilde{\mathrm{p}}} \\ \boldsymbol{v}_{\mathrm{s2},2,\widetilde{\mathrm{p}}} \\ \boldsymbol{v}_{\mathrm{s2},3,\widetilde{\mathrm{p}}} \end{bmatrix} \tag{50}$$

where

$$[\boldsymbol{J}_{k,\widetilde{\mathrm{p}}\lambda}]_{ij} = \frac{\sigma_k + \sigma_{k+1}}{2} (\widetilde{p}_i^{(k)}, \lambda_j^{(k)})_{L^2(\Gamma)} \tag{51}$$

$$[\boldsymbol{D}_{kl,\widetilde{\mathrm{p}}\lambda}]_{ij} = (\widetilde{p}_i^{(k)}, \mathcal{D}_{kl}\, \lambda_j^{(l)})_{L^2(\Gamma)} \tag{52}$$

$$[\boldsymbol{v}_{\mathrm{s2},k,\widetilde{\mathrm{p}}}]_i = -(\widetilde{p}_i^{(k)}, v_{\mathrm{s2}})_{L^2(\Gamma)} \tag{53}$$

and $\phi_{\Gamma_k} \approx \sum_i [\boldsymbol{\phi}_{k,\lambda}]_i \lambda_i^{(k)}$ and $\zeta_l = -(\sigma_{l+1} - \sigma_l)$.

For the sake of completeness, we also consider a mixed discretization for the symmetric formulation. When a mixed discretization is applied to Eq. (23) and Eq. (24), we obtain a rectangular system matrix. To obtain a square system matrix, we propose a slightly modified symmetric formulation given by

$$\begin{aligned} (v_{\mathrm{s},\Omega_{i+1}})\big|_{\Gamma_i} - (v_{\mathrm{s},\Omega_i})\big|_{\Gamma_i} = {} & \sigma_i \mathcal{D}_{i,i-1}\phi_{\Gamma_{i-1}} - (\sigma_i + \sigma_{i+1})\mathcal{D}_{ii}\phi_{\Gamma_i} - (\sigma_i - \sigma_{i+1})\phi_{\Gamma_i} + \sigma_{i+1}\mathcal{D}_{i,i+1}\phi_{\Gamma_{i+1}} \\ & - \mathcal{S}_{i,i-1} d_{\Gamma_{i-1}} + 2\mathcal{S}_{ii} d_{\Gamma_i} + \mathcal{S}_{i,i+1} d_{\Gamma_{i+1}} \end{aligned} \tag{54}$$

and

$$\begin{aligned} (\sigma_i^{-1}\partial_{\hat{\boldsymbol{n}}} v_{\mathrm{s},\Omega_{i+1}})\Big|_{\Gamma_i} - (\sigma_{i+1}^{-1}\partial_{\hat{\boldsymbol{n}}} v_{\mathrm{s},\Omega_i})\Big|_{\Gamma_i} = {} & \mathcal{N}_{i,i-1}\phi_{\Gamma_{i-1}} - 2\mathcal{N}_{ii}\phi_{\Gamma_i} + \mathcal{N}_{i,i+1}\phi_{\Gamma_{i+1}} - \sigma_i^{-1}\mathcal{D}^*_{i,i-1} d_{\Gamma_{i-1}} \\ & + (\sigma_i^{-1} + \sigma_{i+1}^{-1})\mathcal{D}^*_{ii} d_{\Gamma_i} - (\sigma_i^{-1} - \sigma_{i+1}^{-1}) d_{\Gamma_i} - \sigma_{i+1}^{-1}\mathcal{D}^*_{i,i+1} d_{\Gamma_{i+1}} \end{aligned} \tag{55}$$

In the case of three layers, the explicit expression of the resulting linear system is given in Eq. (49), where we use

$$[\boldsymbol{N}_{kl,\widetilde{\lambda}\lambda}]_{ij} = (\widetilde{\lambda}_i^{(k)}, \mathcal{N}_{kl}\lambda_j^{(l)})_{L^2(\Gamma_k)} \tag{56}$$

$$[\boldsymbol{S}_{kl,\widetilde{\mathrm{p}}\mathrm{p}}]_{ij} = (\widetilde{p}_i^{(k)}, \mathcal{S}_{kl} p_j^{(l)})_{L^2(\Gamma_k)} \tag{57}$$

$$[\boldsymbol{D}_{kl,\widetilde{\mathrm{p}}\lambda}]_{ij} = (\widetilde{p}_i^{(k)}, \mathcal{D}_{kl}\lambda_j^{(l)})_{L^2(\Gamma_k)} \tag{58}$$

$$[\boldsymbol{D}^*_{kl,\widetilde{\lambda}\mathrm{p}}]_{ij} = (\widetilde{\lambda}_i^{(k)}, \mathcal{D}^*_{kl} p_j^{(l)})_{L^2(\Gamma_k)} \tag{59}$$

$$[\boldsymbol{v}_{\mathrm{sym},k,\widetilde{\mathrm{p}}}]_i = (\widetilde{p}_i^{(k)}, (v_{\mathrm{s},\Omega_{k+1}})\big|_{\Gamma_k} - (v_{\mathrm{s},\Omega_k})\big|_{\Gamma_k})_{L^2}$$

$$[\boldsymbol{p}_{\mathrm{sym},k,\widetilde{\lambda}}]_i = (\widetilde{\lambda}_i^{(k)}, (\sigma_k^{-1}\partial_{\hat{\boldsymbol{n}}} v_{\mathrm{s},\Omega_{k+1}})\Big|_{\Gamma_k} - (\sigma_{k+1}^{-1}\partial_{\hat{\boldsymbol{n}}} v_{\mathrm{s},\Omega_k})\Big|_{\Gamma_k})_{L^2}$$

with coefficients

$$\alpha_i = (\sigma_i + \sigma_{i+1}), \qquad \beta_i = (\sigma_i - \sigma_{i+1})/2$$
$$\gamma_i = (\sigma_i^{-1} + \sigma_{i+1}^{-1}), \qquad \delta_i = (\sigma_{i+1}^{-1} - \sigma_i^{-1})/2$$

An important point to note is that the BEM equations mentioned above correspond to the interior Neumann problem. Therefore, the potential is only determined up to an additive constant. This gives rise to singular matrices. Hence, an additional condition is needed to solve these systems. The most commonly used one is $\int_\Gamma \phi \mathrm{d}S(\mathbf{r}) = 0$, which corresponds to a surface potential of zero mean. We do not further detail this point given that this is a standard procedure which is widely documented [49,50].

The integrals found in the operators $\mathcal{D}$ and $\mathcal{D}*$ are computed numerically using Gauss quadrature [51] with seven points when the expansion and testing triangle are far from each other. When the expansion and testing triangles are too close, so that the singular kernel cannot be numerically integrated accurately enough, we employ a singularity extraction technique [46] for the inner integrations. For the integration of the $\mathcal{N}$ operator, we follow a standard approach by using its weak formulation such that the derivatives are placed on the testing and expansion functions [36]. The identity operators are always computed analytically.

2. The problem of high conductivity contrast

2.1. Isolated skull approach

As mentioned before, the head is modeled with multilayered compartments of different conductivity (see Fig. 1). Let ω denote the conductivity ratio between two layers. When ω is small (i.e. $\omega < 10$), the double layer and adjoint double layer formulations produce optimum approximation. In the presence of a layer of low conductivity ($\omega > 10$), however, those formulations suffer from numerical inaccuracies. This stems from the fact that the solution scales differently on the interfaces of the head model. Even though conforming discretization improves their accuracy, these formulations yield inaccurate results when the conductivity contrast becomes large. This constitutes a serious drawback given the actual low conductivity of the skull in comparison with the conductivity of the brain and the scalp. In order to overcome this problem, Hamalainen and Sarvas [52] proposed a numerical strategy named Isolated Skull Approach (ISA) for the double layer formulation. This scheme was first formulated for three-layer head model and then generalized to an arbitrary number of layers by [22,53]. The principle of this approach is to write the total potential as a sum of two terms:

$$\phi = \phi_{\mathrm{ISA}} + \phi_{\mathrm{corr}} \tag{60}$$

The first term ϕ_{ISA} is the potential computed assuming an isolated model consisting of only the compartments that are under the skull. The second part ϕ_{corr} is a correction term computed as in the standard double layer formulation with a right-hand side equal to (for three layers model)

$$v_{s3} = \sigma_{\mathrm{skull}}(v_{s2} - \phi_{\mathrm{ISA}}) \tag{61}$$

where σ_{skull} is the conductivity of the skull. We note that ϕ_{ISA} is different from zero only on the surfaces corresponding to the tissues located under the skull. For more details about this approach, we refer the interested reader to [52,22,53]

2.2. Indirect adjoint double layer formulation

While the ISA solves the problem of conductivity ratio for the DL formulation, unfortunately, however, we do not find in the literature a similar way to address this problem for the adjoint double layer formulation. In order to alleviate this shortcoming, we present here a new procedure to compute the potential that we call it Indirect Adjoint Double Layer formulation (IADL). In contrast to the existing adjoint double layer formulation, the new approach allows for computing the electric potential accurately, even in the case of a large dynamic range in the conductivity of the different compartments. The main idea is to write the potential as a contribution of monopole sources J_{Γ_2} and J_{Γ_3} distributed on the two outermost layers. This can formally be written as

$$\phi|_{\Omega_3} = \mathcal{S} J_{\Gamma_2} + \mathcal{S} J_{\Gamma_3} \tag{62}$$

Applying the gradient operator along the normal direction, we get

$$\partial_{\hat{\mathbf{n}}}\phi|_{\Gamma_j} = \pm\frac{J_{\Gamma_j}}{2} + \mathcal{D}^*_{j2} J_{\Gamma_2} + \mathcal{D}^*_{j3} J_{\Gamma_3} \quad \text{for } j = 2, 3 \tag{63}$$

where the sign of $\frac{J_{\Gamma_j}}{2}$ depends on the orientation of the normal. This equation relates the densities J_{Γ_2} and J_{Γ_3} to the current densities. It will be enforced on J_{Γ_2} and J_{Γ_3} such that:

- $\partial_{\hat{\mathbf{n}}}\phi|_{\Gamma_3} = 0$

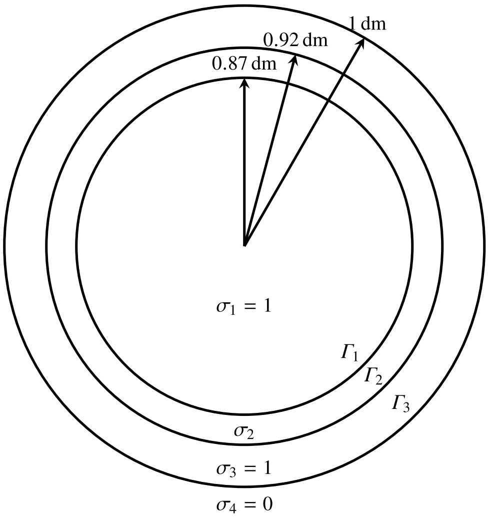

Fig. 5. The multi-layered spherical structure that is used for the evaluation of the different discretizations. Note, that the conductivity σ_2 was varied in parts of the simulations.

•

$$\partial_{\hat{\boldsymbol{n}}}\phi|_{\Gamma_2} = -\frac{1}{2}q_{[}\Gamma_2] + \sum_{i=1}^{N}\mathcal{D}^*_{2i}q_{\Gamma_i} + \partial_{\hat{\boldsymbol{n}}}v_{s1}|_{\Gamma_2} \tag{64}$$

$$= \frac{\sigma_2}{\sigma_3 - \sigma_2}q_{\Gamma_2} \tag{65}$$

where q_{Γ_i} is the solution to the original problem in Eq. (19) on the ith interface. In order to reuse the block matrices of the operator $\mathcal{D}^*$ previously built to solve the original problem of Eq. (19), the densities J_{Γ_2} and J_{Γ_3} are discretized with the same basis functions. Hence, there is no additional computational cost at this stage. By solving this small auxiliary problem (Eq. (63)), the obtained potential shows higher accuracy, independently of the conductivity ratio.

Summarizing, with our new technique, the potential can be computed accurately as follows:

(1) solve the adjoint double layer formulation Eq. (19) to obtain the vector $\boldsymbol{q}$;
(2) solve the auxiliary problem in Eq. (63); for the three-layer head model, it is explicitly given by the following:

$$\begin{bmatrix} -\frac{1}{2}\boldsymbol{I}_{22} + \boldsymbol{D}^*_{22} & \boldsymbol{D}^*_{23} \\ \boldsymbol{D}^*_{32} & \frac{1}{2}\boldsymbol{I}_{33} + \boldsymbol{D}^*_{33} \end{bmatrix} \cdot \underbrace{\begin{bmatrix} \boldsymbol{J}_2 \\ \boldsymbol{J}_3 \end{bmatrix}}_{\boldsymbol{J}_\Gamma} = \begin{bmatrix} \frac{\sigma_2}{\sigma_3-\sigma_2}\boldsymbol{q}_2 \\ \boldsymbol{0} \end{bmatrix} \tag{66}$$

(3) the potential is then given by Eq. (62).

3. Results

To show the practical impact of our newly proposed schemes, we compared them with some of the most common BEM formulations. A first set of comparisons has been obtained on the traditional multi-layered spherical model [54–56]. The reason for this choice is that the analytic solution available for such a model provides a rigorous reference for solidly assessing the numerical performance of all different formulations. This set of comparisons is then complemented by a second one, where we show that our new methods are naturally applicable to MRI-obtained models and that also in this case their performance compares quite favorably with the existing techniques.

3.1. Numerical experiments on a layered spherical head model

The radii of the concentric spheres of the model (Fig. 5) are 0.87 dm, 0.92 dm, and 1 dm. Each sphere is triangulated with an average edge length $h = 0.12$ dm resulting in 1488 elements on the first layer, 1608 elements on the second layer, and 1920 elements on the third layer. The triangulation is uniform delivering a mesh of approximately equally sized and shaped elements. The corresponding (normalized) conductivities are $\sigma_1 = 1$, $\sigma_2 = 1/15$, and $\sigma_3 = 1$, which we abbreviate with the ratio 1:1/15:1 [57]. The source is modeled by a current dipole of magnitude one.

Table 2
The abbreviations and discretizations of the new formulations.

Label	Formulation	Function	
		Expansion	Testing
Mixed discretizations (this work)			
2A	Adjoint double layer	p	$\widetilde{\lambda}$
2B	Double layer	λ	$\widetilde{p}$
2C	New symmetric	p, λ	$\widetilde{p}, \lambda$

Table 3
The abbreviations and discretizations of the new formulations.

Label	Formulation	Function	
		Expansion	Testing
1Bb-ISA	Isolated skull approach	λ	λ
This work:			
2B-ISA	Isolated skull approach	λ	$\widetilde{p}$
1Ab-IA	Indirect adjoint double layer	λ	λ
2A-IA	Indirect adjoint double layer	p	$\widetilde{\lambda}$

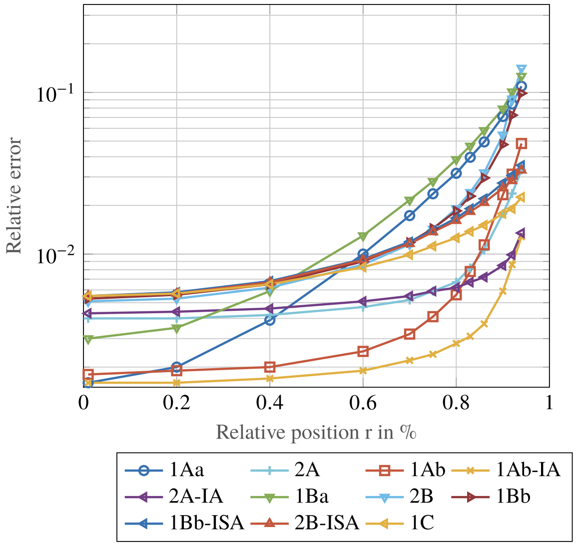

Fig. 6. Relative error as a function of the dipole position inside the sphere Γ_1 with the conductivity $\sigma_2 = 1/15\ \mathrm{S\,m}^1$.

In Tables 1 to 3, we summarize the different discretization strategies and, accordingly, we reference these strategies in the legends of the plots. In the first experiment, the position and orientation of the dipole were the varying factors. Thus, a set of 1200 dipoles were generated and randomly placed at a different radial distance from the center of the spheres. For each dipole position, simulations were run for both radially and tangentially oriented sources. Fig. 6 shows, for different formulations, the mean of the relative error with respect to the analytic solution as a function of the source dipole's eccentricity. We see that, in general, the relative error increases when the dipole approaches the surface $\Gamma 1$. However, the formulations properly discretized are less affected by this phenomenon than other formulations. We also observe that the isolated skull scheme has improved the accuracy of the double layer formulation, similar observations with our new technique IADL. In all cases, adjoint double layer formulations present more accurate results.

In order to observe the variance of the best performing methods, we illustrate in Fig. 7 the boxplot of the relative error as a function of the source depth. We can see that while delivering the most accurate results, the indirect adjoint double layer formulation is also stable having a small variance.

The behavior as well as the accuracy of the different BEM formulations depend on the conductivity ratio of the different compartments of the head. This aspect has been investigated and the results are shown in Fig. 8, displaying the relative error as a function of the electric resistivity $1/\sigma_2$ when the dipole is positioned at 0.83 dm along the x-axis. We observe that the standard non-conforming discretizations of the double layer and the adjoint double layer operator (1Aa and 1Ba) are more strongly impacted by the change of the conductivity σ_2 than the other formulations. The isolated skull approach (ISA) is often used in literature in the presence of a layer of low conductivity to mitigate its impact on the solution error [52,22,53]. Fig. 8 shows also the impact of the use of the ISA technique on both standard formulations and on the mixed dis-

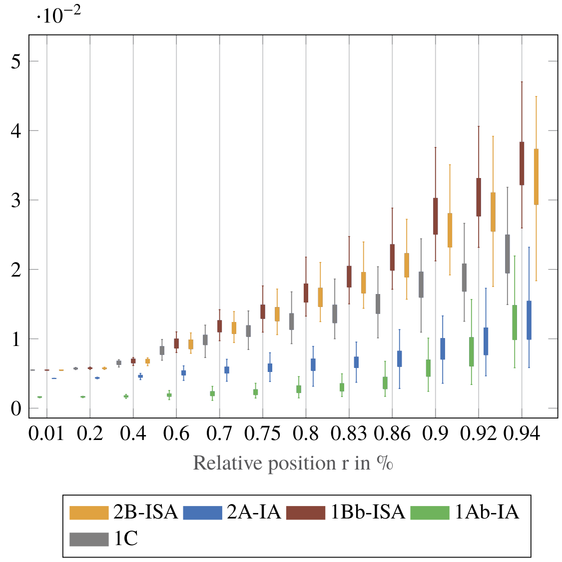

Fig. 7. Relative error as a function of the dipole position inside the sphere Γ_1 with the conductivity $\sigma_2 = 1/15$ S m^1.

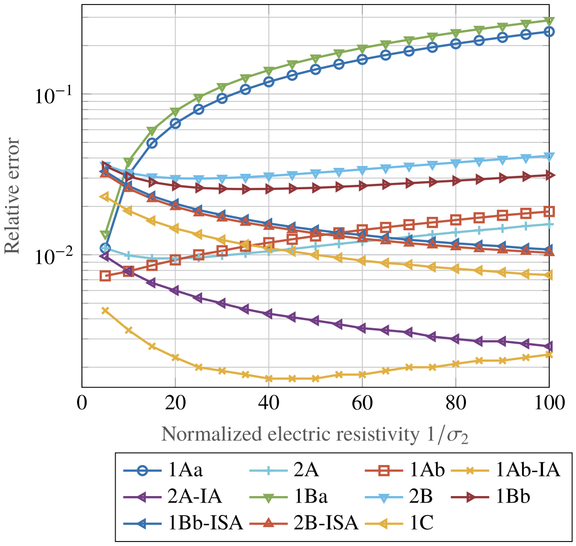

Fig. 8. Relative error as a function of the normalized electric resistivity $1/\sigma_2$ when the dipole is positioned at 0.83 dm along the x-axis.

cretized schemes that we propose in this work. It is found THAT the benefits of the ISA and of the discretization technique we propose are cumulative, and that the two techniques can be perfectly used together. We also see that the symmetric formulation cope well with high conductivity ratios. In addition, we observe that the indirect adjoint double layer formulation is superior in the whole range.

3.2. *Numerical experiments on an MRI-obtained head model*

Although spherical models (and associated analytical solutions) are fundamental for a robust assessment of any newly proposed forward solution strategy, it is of fundamental importance to show the applicability and performance of the technique proposed here on realistic MRI-obtained head models. These models allow for an individual-based head model to be used in solving the forward problem and translates in more precise source localization [6]. Different well-established methods exist in the literature for extracting the cerebral interfaces and are available in several commercial and academic packages including Curry, ScanIP, ASA, BESA, FieldTrip [58], FMRIB [59], FreeSurfer [60], BrainVISA [61], BrainSuite [62], 3D Slicer [63], and BrainVoyager [64]. In our numerical experiment, we have leveraged on BrainSuite to obtain an automatic segmentation of the brain, skull, and scalp. The MRI images used here are a T1-weighted scans of 256 × 256 × 256 cubic voxels (refer to Fig. 9). After following the standard pipeline to reconstruct the surfaces of head tissues, the obtained model

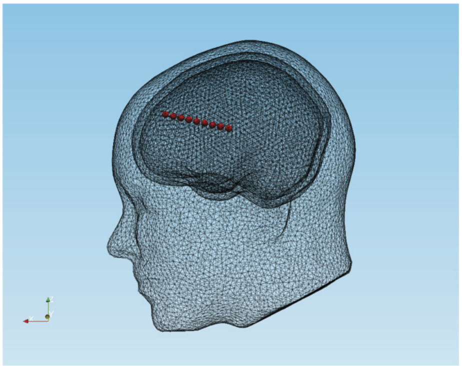

Fig. 9. MRI-based head model: scalp, skull and brain.

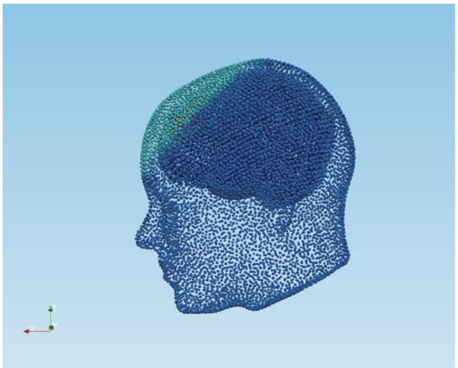

Fig. 10. MRI-based head model: surface potential.

Table 4
Memory and time consumption for the double layer and adjoint double layer discretizations.

Function		CPU (#)	Memory (GB)	Time	
Expansion	Testing			CG (s)	Total (s)
Adjoint double layer discretizations					
p	p	30	12	12	556
p	$\widetilde{\lambda}$	30	12	15	654
λ	λ	30	3	9	765
Double layer discretizations					
p	p	30	12	11	514
λ	$\widetilde{p}$	30	3	7	607
λ	λ	30	3	6	721

is made of 7296, 7296, and 15786 cells for the brain, the skull, and the scalp, respectively. The conductivity of the brain, the skull, and the scalp is $\sigma_1 = 1$, $\sigma_2 = 1/15$, and $\sigma_3 = 1$, respectively.

After the forward problem has been solved, the resulting surface potential can be visualized in Fig. 10. Since the exact solution is unavailable in this case, FEM served as a reference. It was solved on a refined model having 6 million tetrahedrons. The results of this benchmarking can be seen in Fig. 11, where a dipolar source was moved from the center to the surface of the brain as it is shown with red in Fig. 9. The relative error with respect to the reference solution has been computed for all approaches presented in the previous section. We observe that the dual adjoint double layer and the symmetric formulations delivers the most accurate results.

Table 4 summarizes the measurement of the memory and computational time to solve the forward problem. Timing measurements concerns only the adjoint double layer and the double layer formulations with different discretization schemes. The machine used is a Dell server R920 working under windows system. From the table, we conclude that the proposed mixed discretization is not more computationally demanding while complying with the operators mapping properties.

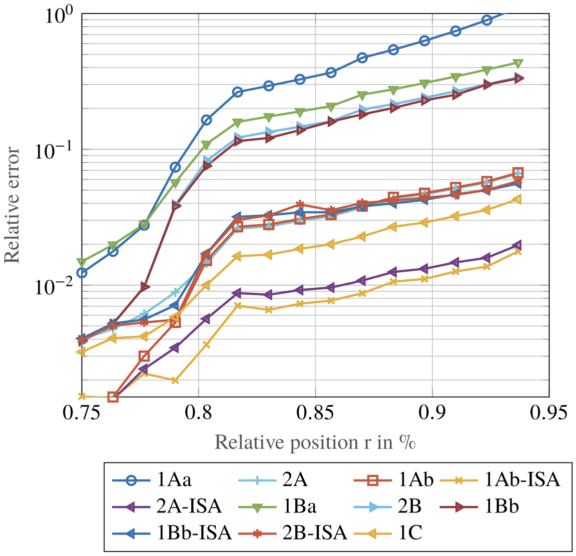

Fig. 11. Head: relative error as a function of the normalized electric resistivity $1/\sigma_2$ when the dipole is positioned at 0.83 dm along the x-axis.

4. Discussion and conclusions

The numerical results confirm that classical, commonly used, discretizations of the integral operators $\mathcal{D}$ and $\mathcal{D}^*$ result in substantially lower level of accuracy than those achievable with their mixed discretized counterparts that we propose here (Figs. 6 and 7). If we then look for the best possible forward problem formulations across all different operators, depending on the scenario (position of the dipole, conductivity), either the mixed discretization or the piece-wise linear PLFs discretization of the adjoint double layer operator (2A and 1Ab) provide the overall best accuracy. The reader should remember, however, that the PLF discretization always comes at the price of an increase in the computational burden. Moreover, every time the dipolar brain source comes close to a brain layer interface, we find that the mixed discretization yields always comparable accuracy with the PLF discretization.

We varied the conductivity over a wide range of values. In recent reports, the conductivity ratio of brain, skull, and scalp is estimated from in vivo measurements to be between 1:1/15:1 and 1:1/25:1, and the ratio 1:1/80:1 arising from in vitro measurements and which until recently has been used in neuroimaging applications is currently questioned [65,66,57,67]. We have observed that, for the relevant range of in vivo measured conductivities, a straightforward application of double layer and adjoint double layer formulation leads to a poor accuracy. The application of ISA technique to both standard formulations and on the mixed discretized schemes substantially improves their accuracy. We also observed that the new integral representation (IADL) yields the highest accuracy compared with other methods (see Fig. 8).

From our experiments, it is evident that also the symmetric formulation performs quite well when the dipole is near the surface (see Figs. 6 and 7). This is consistent with the theoretical consideration that the symmetric formulation is a conformingly discretized scheme. However, it should be noted that the symmetric formulation comes at the cost of a considerable computational burden. The dimension of the system matrix is one and a half times the size of the matrices of the mixed discretization. Thus the symmetric formulation is comparatively less competitive in the source localization process, where the propagation model needs to be calculated many times.

For the sake of completeness, we also presented a mixed discretization of the symmetric formulation. No advantages were observed, since the original symmetric formulation was already discretized conformingly, and the obtained system is plagued with the same drawbacks as the original symmetric formulation. We note also that the application of the isolated skull approach improves the accuracy of the solution, especially for shallow dipoles. The improvement, however, comes at the cost of some additional computations.

In conclusion, the numerical results confirm what can be theoretically expected, i.e. that mixed and conforming discretizations provide formulations with a higher level of accuracy of their standard counterparts. Moreover the adjoint double layer operator provides often the global optimum across all operators and discretizations. Taking into account that the computational costs of the mixed discretization is lower than those of higher order alternatives, the discretizations schemes proposed here can be a very competitive new option among all EEG forward formulations.

Acknowledgements

This work was supported in part by the “Agence nationale de la recherche”, under Project FASTEEG-ANR-12-JS09-0010, in part by the European Union Project NEUROIMAGEEG, in part by the CominLabs excellence laboratory, managed by the

National Research Agency in the “Investing for the Future” program under reference ANR-10-LABX-07-01, project SABRE, and in part by the European Research Council (ERC) under the European Union’s Horizon 2020 research and innovation program (ERC project 321, grant No. 724846).

Appendix A. Relevant Sobolev spaces

This appendix contains the definitions of the Sobolev spaces used in this paper. The presentation is concise for the sake of brevity; the interested reader could refer to [68] for further details on the topic.

The Sobolev space $H^1(\Omega)$ is defined as

$$H^1(\Omega) = \{f : \Omega \to \mathbb{R} \mid f \in L^2(\Omega) \wedge \nabla f \in (L^2(\Omega))^3\}$$

The space L^2 is the set of all equivalence classes of functions that are square integrable in the Lebesgue sense:

$$L^2(\Omega) = \{f : \Omega \to \mathbb{R} \mid \|f\|_{L^2(\Omega)} < \infty\} \tag{67}$$

with the L^2-norm defined as

$$\|f\|_{L^2(\Omega)} = (\int_\Omega |f(\mathbf{r})|^2 \mathrm{d}\mathbf{r})^{1/2} \tag{68}$$

From the space $H^1(\Omega)$, we can define the fractional-order Sobolev space $H^{1/2}(\Gamma)$ as

$$H^{1/2}(\Gamma) = \{f : \Gamma \to \mathbb{R} \mid \exists g \in H^1(\Omega) \text{ so that } g|_\Gamma = f\}$$

The space $H^{-1/2}(\Gamma)$ is the topological dual space of $H^{1/2}(\Gamma)$, that is, the space that contains all the linear and continuous functionals that map the functions of $H^{1/2}(\Gamma)$ to $\mathbb{R}$ [68].

Appendix B. The representation theorem

The representation theorem allows one to represent the solution u of the Laplace equation on a domain Ω in terms of its boundary values [69].

Theorem 1. *Let $\Omega^- \subset \mathbb{R}^3$ be an open, connected set with smooth boundary Γ, $\Omega^+ = \mathbb{R}^3 \setminus \overline{\Omega^-}$ its complement. Let $\Delta u = 0$ in $\Omega = \Omega^+ \cup \Omega^-$, and let u satisfy the conditions*

$$\lim_{r\to\infty} r|u(\mathbf{r})| < \infty \tag{69}$$

$$\lim_{r\to\infty} r\frac{\partial u}{\partial r}(\mathbf{r}) = 0 \tag{70}$$

where $r = \|\mathbf{r}\|$. We define $p = \partial_{\hat{\mathbf{n}}} u$. Then it holds

$$-p = +\mathcal{N}[u] - \mathcal{D}^*[p], \quad \text{for } \mathbf{r} \in \Omega \tag{71}$$

$$u = -\mathcal{D}[u] + \mathcal{S}[p], \quad \text{for } \mathbf{r} \in \Omega \tag{72}$$

$$-p|_\Gamma^\pm = +\mathcal{N}[u] + (\pm\mathcal{I}/2 - \mathcal{D}^*)[p], \quad \text{for } \mathbf{r} \in \Gamma \tag{73}$$

$$u|_\Gamma^\pm = (\mp\mathcal{I}/2 - \mathcal{D})[u] + \mathcal{S}[p], \quad \text{for } \mathbf{r} \in \Gamma \tag{74}$$

where $\mathcal{I}$ is the identity operator and the operators $\mathcal{S}$, $\mathcal{D}$, $\mathcal{D}^*$, and $\mathcal{N}$ are defined in Eqs. (8) to (11).

Whenever $[u]$ or $[p]$, respectively, are zero, we obtain

$$p|_\Gamma^\pm = \mp[p]/2 + \mathcal{D}^*[p], \quad \text{for } \mathbf{r} \in \Gamma \tag{75}$$

and

$$u|_\Gamma^\pm = \mp[u]/2 - \mathcal{D}[u], \quad \text{for } \mathbf{r} \in \Gamma \tag{76}$$

The representation theorem holds also in the presence of multilayered structures as depicted in Fig. 1. Let ξ_{Γ_i} and μ_{Γ_i} be functions defined on the ith surface. We define the potentials $u_{\mathrm{h}1} = \sum_{i=1}^N \mathcal{S}\xi_{\Gamma_i}$ and $u_{\mathrm{h}2} = \sum_{i=1}^N \mathcal{D}\mu_{\Gamma_i}$. Then we obtain

$$\partial_{\hat{\boldsymbol{n}}} u_{\mathrm{h}1}^{\pm}(\boldsymbol{r}) = \mp\xi_{\Gamma_j}/2 + \sum_{i=1}^{N} \mathcal{D}_{ji}^{*}\xi_{\Gamma_i} \quad \text{for } \boldsymbol{r} \in \Gamma_j \tag{77}$$

$$u_{\mathrm{h}2}^{\pm}(\boldsymbol{r}) = \pm\mu_{\Gamma_j}/2 + \sum_{i=1}^{N} \mathcal{D}_{ji}\mu_{\Gamma_i} \quad \text{for } \boldsymbol{r} \in \Gamma_j \tag{78}$$

References

[1] Z.A. Acar, C.E. Acar, S. Makeig, Simultaneous head tissue conductivity and EEG source location estimation, NeuroImage 124 (2016) 168–180.

[2] M. Siems, A.-A. Pape, J.F. Hipp, M. Siegel, Measuring the cortical correlation structure of spontaneous oscillatory activity with EEG and MEG, NeuroImage (2016).

[3] K. Peng, D.K. Nguyen, P. Vannasing, J. Tremblay, F. Lesage, P. Pouliot, Using patient-specific hemodynamic response function in epileptic spike analysis of human epilepsy: a study based on EEG–fNIRS, NeuroImage 126 (2016) 239–255.

[4] J. Dabek, K. Kalogianni, E. Rotgans, F.C. van der Helm, G. Kwakkel, E.E. van Wegen, A. Daffertshofer, J.C. de Munck, Determination of head conductivity frequency response in vivo with optimized EIT-EEG, NeuroImage (2015).

[5] C.-G. Bénar, D. Schön, S. Grimault, B. Nazarian, B. Burle, M. Roth, J.-M. Badier, P. Marquis, C. Liegeois-Chauvel, J.-L. Anton, Single-trial analysis of oddball event-related potentials in simultaneous EEG-fMRI, Hum. Brain Mapp. 28 (7) (2007) 602–613.

[6] Y. Huang, L.C. Parra, S. Haufe, The New York head—a precise standardized volume conductor model for EEG source localization and TES targeting, NeuroImage (2015).

[7] J. Jorge, F. Grouiller, R. Gruetter, W. Van Der Zwaag, P. Figueiredo, Towards high-quality simultaneous EEG-fMRI at 7 T: detection and reduction of EEG artifacts due to head motion, NeuroImage 120 (2015) 143–153.

[8] L. Fiederer, J. Vorwerk, F. Lucka, M. Dannhauer, S. Yang, M. Dümpelmann, A. Schulze-Bonhage, A. Aertsen, O. Speck, C. Wolters, et al., The role of blood vessels in high-resolution volume conductor head modeling of EEG, NeuroImage 128 (2016) 193–208.

[9] C. Phillips, M.D. Rugg, K.J. Friston, Systematic regularization of linear inverse solutions of the EEG source localization problem, NeuroImage 17 (1) (2002) 287–301.

[10] L. Koessler, C. Benar, L. Maillard, J.-M. Badier, J.P. Vignal, F. Bartolomei, P. Chauvel, M. Gavaret, Source localization of ictal epileptic activity investigated by high resolution EEG and validated by sEEG, NeuroImage 51 (2) (2010) 642–653.

[11] R. Grech, T. Cassar, J. Muscat, K.P. Camilleri, S.G. Fabri, M. Zervakis, P. Xanthopoulos, V. Sakkalis, B. Vanrumste, Review on solving the inverse problem in EEG source analysis, J. NeuroEng. Rehabil. 5 (1) (2008) 25.

[12] R.D. Pascual-Marqui, Review of methods for solving the EEG inverse problem, Int. J. Bioelectromagn. 1 (1) (1999) 75–86.

[13] Z.A. Acar, S. Makeig, Effects of forward model errors on EEG source localization, Brain Topogr. 26 (3) (2013) 378–396.

[14] H. Hallez, B. Vanrumste, R. Grech, J. Muscat, W. De Clercq, A. Vergult, Y. D'Asseler, K.P. Camilleri, S.G. Fabri, S. Van Huffel, et al., Review on solving the forward problem in EEG source analysis, J. NeuroEng. Rehabil. 4 (1) (2007) 46.

[15] H. Hallez, B. Vanrumste, R. Grech, J. Muscat, W. De Clercq, A. Vergult, Y. D'Asseler, K.P. Camilleri, S.G. Fabri, S. Van Huffel, et al., Review on solving the forward problem in EEG source analysis, J. NeuroEng. Rehabil. 4 (1) (2007) 46.

[16] B. He, T. Musha, Y. Okamoto, S. Homma, Y. Nakajima, T. Sato, Electric dipole tracing in the brain by means of the boundary element method and its accuracy, IEEE Trans. Biomed. Eng. 6 (1987) 406–414.

[17] M. Fuchs, M. Wagner, J. Kastner, Boundary element method volume conductor models for EEG source reconstruction, Clin. Neurophysiol. 112 (8) (2001) 1400–1407.

[18] B. He, Y. Wang, D. Wu, Estimating cortical potentials from scalp EEGs in a realistically shaped inhomogeneous head model by means of the boundary element method, IEEE Trans. Biomed. Eng. 46 (10) (1999) 1264–1268.

[19] D. Cosandier-Rimélé, I. Merlet, J.-M. Badier, P. Chauvel, F. Wendling, The neuronal sources of EEG: modeling of simultaneous scalp and intracerebral recordings in epilepsy, NeuroImage 42 (1) (2008) 135–146.

[20] M. Fuchs, R. Drenckhahn, H. Wischmann, M. Wagner, An improved boundary element method for realistic volume-conductor modeling, IEEE Trans. Biomed. Eng. 45 (8) (1998) 980–997.

[21] B. Yvert, A. Crouzeix-Cheylus, J. Pernier, Fast realistic modeling in bioelectromagnetism using lead-field interpolation, Hum. Brain Mapp. 14 (1) (2001) 48–63.

[22] J.W. Meijs, O.W. Weier, M.J. Peters, A. van Oosterom, On the numerical accuracy of the boundary element method (EEG application), IEEE Trans. Biomed. Eng. 36 (10) (1989) 1038–1049.

[23] F. Zanow, M. Peters, Individually shaped volume conductor models of the head in EEG source localisation, Med. Biol. Eng. Comput. 33 (4) (1995) 582–588.

[24] G. Adde, M. Clerc, O. Faugeras, R. Keriven, J. Kybic, T. Papadopoulo, Symmetric BEM formulation for the m/EEG forward problem, in: Information Processing in Medical Imaging, Springer, 2003, pp. 524–535.

[25] J. Kybic, M. Clerc, T. Abboud, O. Faugeras, R. Keriven, T. Papadopoulo, A common formalism for the integral formulations of the forward EEG problem, IEEE Trans. Med. Imaging 24 (1) (2005) 12–28.

[26] O. Scherzer, Handbook of Mathematical Methods in Imaging, vol. 1, Springer Science & Business Media, 2011.

[27] C.H. Wolters, H. Köstler, C. Möller, J. Härdtlein, L. Grasedyck, W. Hackbusch, Numerical mathematics of the subtraction method for the modeling of a current dipole in EEG source reconstruction using finite element head models, SIAM J. Sci. Comput. 30 (1) (2007) 24–45.

[28] S.A. Sauter, C. Schwab, Boundary Element Methods, Springer, 2011.

[29] K. Cools, F.P. Andriulli, F. Olyslager, E. Michielssen, Improving the mfie's accuracy by using a mixed discretization, in: IEEE Antennas and Propagation Society International Symposium, 2009, APSURSI'09, IEEE, 2009, pp. 1–4.

[30] K. Cools, F. Andriulli, D. De Zutter, E. Michielssen, Accurate and conforming mixed discretization of the MFIE, IEEE Antennas Wirel. Propag. Lett. 10 (2011) 528–531.

[31] S. Yan, J.-M. Jin, Z. Nie, Improving the accuracy of the second-kind Fredholm integral equations by using the Buffa–Christiansen functions, IEEE Trans. Antennas Propag. 59 (4) (2011) 1299–1310.

[32] P. Ylä-Oijala, S.P. Kiminki, S. Järvenpää, Conforming boundary element methods in acoustics, Eng. Anal. Bound. Elem. 50 (2015) 447–458.

[33] L. Rahmouni, F. Andriulli, Mixed discretization formulations for the direct EEG problem, in: 2014 8th European Conference on Antennas and Propagation, EuCAP, April 2014, pp. 3183–3185.

[34] G. Pruis, B.H. Gilding, M. Peters, A comparison of different numerical methods for solving the forward problem in EEG and MEG, Physiol. Meas. 14 (4A) (1993), A1.

[35] G. Huiskamp, M. Vroeijenstijn, R. van Dijk, G. Wieneke, A.C. van Huffelen, The need for correct realistic geometry in the inverse EEG problem, IEEE Trans. Biomed. Eng. 46 (11) (1999) 1281–1287.

[36] O. Steinbach, Numerical Approximation Methods for Elliptic Boundary Value Problems. Finite and Boundary Elements, 2008.
[37] J. De Munck, B. Van Dijk, H. Spekreijse, Mathematical dipoles are adequate to describe realistic generators of human brain activity, IEEE Trans. Biomed. Eng. 35 (11) (1988) 960–966.
[38] J. Sarvas, Basic mathematical and electromagnetic concepts of the biomagnetic inverse problem, Phys. Med. Biol. 32 (1) (1987) 11.
[39] P.H. Schimpf, C. Ramon, J. Haueisen, Dipole models for the EEG and MEG, IEEE Trans. Biomed. Eng. 49 (5) (2002) 409–418.
[40] M. Stenroos, J. Sarvas, Bioelectromagnetic forward problem: isolated source approach revis(it)ed, Phys. Med. Biol. 57 (11) (2012) 3517.
[41] A. Gramfort, M. Luessi, E. Larson, D.A. Engemann, D. Strohmeier, C. Brodbeck, L. Parkkonen, M.S. Hämäläinen, MNE software for processing MEG and EEG data, NeuroImage 86 (2014) 446–460.
[42] G. Birot, L. Spinelli, S. Vulliémoz, P. Mégevand, D. Brunet, M. Seeck, C.M. Michel, Head model and electrical source imaging: a study of 38 epileptic patients, NeuroImage: Clinical 5 (2014) 77–83.
[43] O. Steinbach, W.L. Wendland, The construction of some efficient preconditioners in the boundary element method, Adv. Comput. Math. 9 (1–2) (1998) 191–216.
[44] W. Hackbusch, Integral Equations: Theory and Numerical Treatment, vol. 120, Birkhäuser, 2012.
[45] R.D. Graglia, Static and dynamic potential integrals for linearly varying source distributions in two-and three-dimensional problems, IEEE Trans. Antennas Propag. 35 (6) (1987) 662–669.
[46] R.D. Graglia, On the numerical integration of the linear shape functions times the 3-d Green's function or its gradient on a plane triangle, IEEE Trans. Antennas Propag. 41 (10) (1993) 1448–1455.
[47] J. De Munck, A linear discretization of the volume conductor boundary integral equation using analytically integrated elements, IEEE Trans. Biomed. Eng. 39 (9) (1992) 986–990.
[48] A. Buffa, S. Christiansen, A dual finite element complex on the barycentric refinement, Math. Comput. 76 (260) (2007) 1743–1769.
[49] J. Rahola, S. Tissari, Iterative solution of dense linear systems arising from the electrostatic integral equation in MEG, Phys. Med. Biol. 47 (6) (2002) 961.
[50] T.F. Chan, Deflated decomposition of solutions of nearly singular systems, SIAM J. Numer. Anal. 21 (4) (1984) 738–754.
[51] D. Dunavant, High degree efficient symmetrical Gaussian quadrature rules for the triangle, Int. J. Numer. Methods Eng. 21 (6) (1985) 1129–1148.
[52] M.S. Hamalainen, J. Sarvas, Realistic conductivity geometry model of the human head for interpretation of neuromagnetic data, IEEE Trans. Biomed. Eng. 36 (2) (1989) 165–171.
[53] N.G. Gençer, Z. Akalin-Acar, Use of the isolated problem approach for multi-compartment BEM models of electro-magnetic source imaging, Phys. Med. Biol. 50 (13) (2005) 3007.
[54] J. De Munck, The potential distribution in a layered anisotropic spheroidal volume conductor, J. Appl. Phys. 64 (2) (1988) 464–470.
[55] d.J. Munck, M.J. Peters, A fast method to compute the potential in the multisphere model, IEEE Trans. Biomed. Eng. 40 (11) (1993) 1166–1174.
[56] Z. Zhang, A fast method to compute surface potentials generated by dipoles within multilayer anisotropic spheres, Phys. Med. Biol. 40 (3) (1995) 335.
[57] T.F. Oostendorp, J. Delbeke, D.F. Stegeman, The conductivity of the human skull: results of in vivo and in vitro measurements, IEEE Trans. Biomed. Eng. 47 (11) (2000) 1487–1492.
[58] R. Oostenveld, P. Fries, E. Maris, J.-M. Schoffelen, Fieldtrip: open source software for advanced analysis of MEG, EEG, and invasive electrophysiological data, Comput. Intell. Neurosci. 2011 (2010).
[59] S.M. Smith, Fast robust automated brain extraction, Hum. Brain Mapp. 17 (3) (2002) 143–155.
[60] B. Fischl, A. van der Kouwe, C. Destrieux, E. Halgren, F. Ségonne, D.H. Salat, E. Busa, L.J. Seidman, J. Goldstein, D. Kennedy, et al., Automatically parcellating the human cerebral cortex, Cereb. Cortex 14 (1) (2004) 11–22.
[61] D. Geffroy, D. Rivière, I. Denghien, N. Souedet, S. Laguitton, Y. Cointepas, Brainvisa: a complete software platform for neuroimaging, in: Python in Neuroscience Workshop, Euroscipy, Paris, 2011.
[62] D.W. Shattuck, R.M. Leahy, Brainsuite: an automated cortical surface identification tool, Med. Image Anal. 6 (2) (2002) 129–142.
[63] A. Fedorov, R. Beichel, J. Kalpathy-Cramer, J. Finet, J.-C. Fillion-Robin, S. Pujol, C. Bauer, D. Jennings, F. Fennessy, M. Sonka, et al., 3d slicer as an image computing platform for the quantitative imaging network, Magn. Reson. Imaging 30 (9) (2012) 1323–1341.
[64] R. Goebel, Brainvoyager—past, present, future, NeuroImage 62 (2) (2012) 748–756.
[65] S. Gonçalves, J.C. De Munck, J. Verbunt, F. Bijma, R.M. Heethaar, F. Lopes da Silva, et al., In vivo measurement of the brain and skull resistivities using an EIT-based method and realistic models for the head, IEEE Trans. Biomed. Eng. 50 (6) (2003) 754–767.
[66] Y. Zhang, W. van Drongelen, B. He, Estimation of in vivo brain-to-skull conductivity ratio in humans, Appl. Phys. Lett. 89 (22) (2006) 223903.
[67] M. Clerc, G. Adde, J. Kybic, T. Papadopoulo, J.-M. Badier, In vivo conductivity estimation with symmetric boundary elements, Int. J. Bioelectromagn. 7 (2005) 307–310.
[68] L. Tartar, An Introduction to Sobolev Spaces and Interpolation, Springer, 2007.
[69] J.-C. Nédélec, Acoustic and Electromagnetic Equations: Integral Representations for Harmonic Problems, vol. 144, Springer, 2001.